
Article:
Yue, X, Zhang, L, Ma, L et al. (2021) Influence of a small velocity variation on the evolution of the corrosion products and corrosion behaviour of super 13Cr SS in a geothermal CO2 containing environment. Corrosion Science, 178. 108983. ISSN: 0010-938X

https://doi.org/10.1016/j.corsci.2020.108983

Influence of a small velocity variation on the evolution of the corrosion products and corrosion behaviour of super 13Cr SS in a geothermal CO_2 containing environment

Xiaoqi Yue[a, b, c], Lei Zhang[b], Lei Ma[d], Minxu Lu[b], Anne Neville[a] and Yong Hua[a]*

a: Institute of Functional Surfaces, School of Mechanical Engineering, University of Leeds, Leeds, LS2 9JT, United Kingdom.

b: Institute of Advanced Materials and Technology, University of Science and Technology Beijing, 30 Xueyuan road, Beijing, 100083, China.

c: Shunde Graduate School, University of Science and Technology Beijing, Foshan, 528399, China

d: PetroChina Tarim Oilfield Company, Research Institute of Oil and Gas Engeineering, Korla, 841000, China.

*Corresponding author: Yong Hua, Email: Y.Hua@leeds.ac.uk

Abstract

The general and localised corrosion of super 13Cr SS under various CO_2 partial pressures (p_{CO2}) in the static conditions and rotated speeds of 188 rpm at 200°C were evaluated. The results show that super 13Cr SS exhibited lower localised corrosion risk at 188 rpm compared to the static conditions. The small velocity retarded the localised corrosion through the formation of uniform corrosion product scales, which mainly comprised nanocrystalline $FeCr_2O_4$ at 2.7 bar p_{CO2}. A double-layered film consisted of an inner layer of $Cr(OH)_3$/undissolved austenite and an outer crystalline $FeCO_3$ layer was observed at 28.5 bar p_{CO2}.

Keywords: super 13Cr SS, velocity, CO_2 corrosion, $FeCr_2O_4$

Introduction

Stainless steel (SS) has been widely used since it was invented based on its passivity induced noble behaviour [1]. Passivity is attributed to the presence of the high level of alloying elements such as chromium [2,3], nickel, and molybdenum [4,5]. SS generally contains higher

alloying content i.e. 18% Cr, 13% Ni and 2–3% Mo as the required resistance to corrosion is increased. Optimise the cost of using high-alloy SS is considered as a key driver for arduous conditions such as the geothermal applications or in high temperature oil and gas wells.

Super 13Cr SS was developed as a martensitic SS to achieve comparable excellent corrosion resistance and mechanical properties to austenitic SS but with reduced the cost through reducing the nickel and molybdenum content to 5% and 2%, respectively. Super 13Cr SS has been considered as one of the suitable materials for the downhole/geothermal fields [6–9].

The ability to form passive film is the primary characteristic of SS, it provides protectiveness and determines the corrosion resistance of materials exposed to a corrosive solution [5]. In general, the passive film on the SS surface is formed via the following reactions:

$$2Cr(OH)_3 \leftrightarrow Cr_2O_3 + 3H_2O \quad (1)$$

$$2Cr + 3H_2O \leftrightarrow Cr_2O_3 + 6H^+ + 6e^- \quad (2)$$

$$Cr + 3H_2O \leftrightarrow Cr(OH)_3 + 3H^+ + 3e^- \quad (3)$$

Despite the excellent corrosion resistance as well as the superior mechanical properties, super 13Cr SS is still proving to corrosion especially at high temperatures [10–12]. Understanding the limitation of the super 13Cr SS in different aggressive environments is important. At high temperatures, the passive film is often unstabilised and allows the accelerated diffusion of metal ions from matrix to the solution [13]. This is reflected in the observed degradation of passive films during the corrosion processes at high temperatures [14].

Corrosion product scales play a crucial role in defining the corrosion resistance of the underlying steel [15–20]. The corrosion product family is composed of passive films (Cr_2O_3/$Cr(OH)_3$), oxide and/or hydroxide films ($FeCr_2O_4$, $Cr(OH)_3$) as well as the outer carbonate layers such as $FeCO_3$.

The formation of $FeCr_2O_4$ may form on the surface via the following reactions [19,21,22]:

$$Fe + 2Cr + 4H_2O \rightarrow FeCr_2O_4 + 8H^+ + 8e^- \quad (4)$$

$$Fe^{2+} + Cr_2O_3 + H_2O \leftrightarrow FeCr_2O_4 + 2H^+ \quad (5)$$

$$Fe^{2+} + 2Cr(OH)_3(aq) \leftrightarrow FeCr_2O_4 + 2H^+ + 2H_2O \quad (6)$$

The development of crystalline $FeCO_3$ can occur not only via the one-stage process directly with carbonates [23];

$$Fe^{2+} + CO_3^{2-} \rightarrow FeCO_3 \quad (7)$$

but also two-stage reactions with bicarbonates [24,25]:

$$Fe^{2+} + 2HCO_3^- \rightarrow Fe(HCO_3)_2 \quad (8\text{-}1)$$

$$Fe(HCO_3)_2 \rightarrow FeCO_3 + CO_2 + H_2O \quad (8\text{-}2)$$

The reduction in corrosion rate is ascribed to the development of corrosion product scales, this layer blocks the corrosive species pathway and acts as a diffusion barrier to electrochemically-active species. The chemical/physical properties and the degree of corrosion product protection are evidenced to change with different brine compositions [26–28] and the corrosion products with nanosized features can normally indicate better corrosion resistance based on the highly dense and compact nature [16,29,30].

The bulk of research has been directed towards understanding the evolution mechanisms of the corrosion scales or the corrosion behaviour of super 13Cr SS in static conditions [12,31–34]. There is a consensus from the literature that the growth of protective corrosion products enhances the corrosion resistance of super 13Cr SS. Moreira et al. [18] studied the electrochemical behaviour of super 13Cr SS between 0.1 hours and 75 hours in a NaCl brine at a temperature of 175°C, they recorded that the corrosion rate was maintained at a low level and suggested that the super 13Cr SS did not suffer destructive damage in these conditions. The increase of impedance indicated that corrosion films were detected after a long-term exposure time; however, their study did not clarify the composition and structural evolution of the corrosion films. Li et al. [34] used additional surface analysis methods in their study where super 13Cr SS was immersed in a NaCl solution saturated with CO_2 at 180°C. They observed that the growth of the corrosion scales was rapidly at 180°C and developed into thick layers (mainly consisting of $Cr(OH)_3$(s) and Cr_2O_3(s)). Furthermore, Zhao et al. [19] reported that the content of $Cr(OH)_3$(s) becomes particularly high as increasing temperature and pressure. A recent study conducted by Yue et al. [14] revealed that the corrosion product

scales are capable of reducing the corrosion rates. The increased protection of super 13Cr SS was related to the presence of a double-layered film which consisted of an inner layer of $FeCr_2O_4$ and an outer $FeCO_3$ layer. The inner layer was believed to provide better corrosion protection compared to the outer $FeCO_3$ layer.

Numbers of researchers have highlighted the flow speed affecting the corrosion product morphology, precipitation kinetics, and mechanical properties [16,35–37], and have considered that dynamic conditions can avoid or delay the development of corrosion product scales. The breakdown of the corrosion product scales caused by flow in actual downhole/geothermal field production has already been identified as a mechanism of corrosion by Han et al. [38], who used a rotating disk electrode to keep the system flowing. Zhao et al. [16] indicated that the flow delayed the precipitation of amorphous $Cr(OH)_3(s)$ within the corrosion products, and increased the boundaries between Cr_2O_3 and $Cr(OH)_3(s)$, causing the diffusion pathways to increase and consequently causing higher pitting corrosion risk. So far, literature has discussed the temperature, p_{CO_2}, and chloride ion concentration issues relating to CO_2 corrosion mechanisms and the growth mechanisms of the corrosion product scales for super 13Cr SS [18,20,7,11,39]; However, little research has focused on the protective capabilities of the corrosion product scales under flowing conditions and the flow-induced effect on localised corrosion.

Based on the above literature review, this paper is focused towards the corrosion behaviour in terms of general and localised corrosion of super 13Cr SS in dynamic conditions compared to static conditions. It discusses the formation mechanism and protective behaviour of the corrosion scales by applying a small flow rate at high temperature and different p_{CO_2} values for the downhole/geothermal environments.

Experimental

2.1. Material and Methods

Super 13Cr SS specimens, with a surface area of 25 mm x 13 mm and 3 mm thick, were used in the following experiments. The measured compositions of the material are 12.80 wt.% Cr, 1.92 wt.% Mo, 4.78 wt.% Ni, $\leqslant$0.001 wt.% S, $\leqslant$0.001 wt.% P, 0.34 wt.% Mn, 0.04 wt.% C,

and balance Fe. The sample surface was grinding to 600 # (R_a=0.064 μm) by silicon carbide paper, then rinsing with acetone, ethanol, and deionized (DI) water, respectively, following by hot-air drying. The prepared samples were kept in a desiccator and weighed (W_0) on an electronic balance to within an accuracy of 10^{-5} g before being put inside the autoclave. All the corrosion experiments are performed within a C-276 alloy dynamic autoclave as shown in Figure 1.

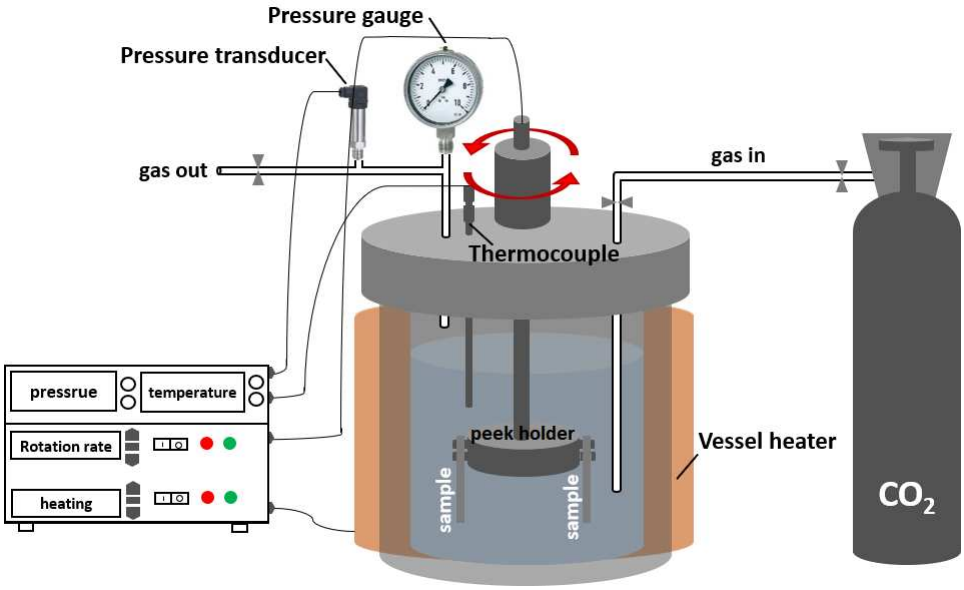

Figure 1. The experimental set up of the system

Prior to the test, the samples were fixed to a sample holder (screws and sample holder are made of PEEK, in order to avoid the galvanic effect to the tested materials) in the autoclave, the whole system was purged with high-pressure CO_2 (99.999%), then the de-aerated (<10 ppb [40]) CO_2-saturated (1 bar) 4.86 wt.% NaCl solution was carefully transferred into the closed autoclave using a shoe suction pump at room pressure and temperature. The solution was pressurised to the required pressure and then heated to 200°C. The cooling time was controlled within 10 minutes from the end of the experiments. The various evaluated test conditions and calculated pH values (MultiScale software [41]) are provided in Table 1. Within this work, the rotation speed of 188 rpm was considered, which the corresponding flow velocity was 0.25 m/s and laminar flow via Eq. S2 and Eq. S3 as shown in the supplementary document.

Table 1: Test matrix at 200 °C and various p_{CO_2}

Concentration of component in brine (mg/L)	Temp /°C	Rotate speed/rpm	CO_2 pressure at 25°C/bar	pH	p_{CO_2}/ bar	Total pressure /bar	Immersion time/hour
Cl^-: 29503, HCO_3^-: 585,	200	0/188	1	6.41	2.7	18	5
							20
							48
							120
		0/188	20	5.39	28.5	45	5
							20
							48
							120

After the experiments, DI-water was used to rinse the extracted samples, then dried, and removal of corrosion scales follow ASTM G1-03 standard (Designation C.3.1) [42]. The corrosion rate (C_R) was calculated in mm/year via Eq. (9), which was obtained according to Eq. S4 and Eq. S5 as shown in the supplementary document.

$$C_R = \frac{87600(W_0 - W)}{t\rho A} \quad (9)$$

Where W represents the sample weight after mass loss, t, ρ, and A are the immersion time in hours, the steel density in g/cm^3, and the exposed surface area in cm^2, respectively.

2.2. Corrosion product analysis

The top-view and cross-sectional morphology of the corrosion product scales was observed using Scanning Electron Microscope (SEM). The assessment of the different crystalline corrosion products was done at various p_{CO_2} and immersion times via X-Ray Diffraction (XRD) spectrum and Raman spectroscopy. The cross-sectional samples were cut from the tested specimens by the Focused Ion Beam (FIB). More detailed experimental procedures for corrosion product analysis can be found in our previous publication [14, 36].

Results

The comparisons of averaged corrosion rate measurements in a static condition and a rotation speed of 188 rpm at various p_{CO_2}

Figure 2 shows the averaged corrosion rates of super 13Cr SS exposed to the brine for different immersion times at 200°C and p_{CO_2} of 2.7 bar and 28.5 bar, respectively. For both

static and dynamic conditions at low p_{CO_2} of 2.7 bar (Figure 1a), high corrosion rates are recorded after the first 5 hours and they decreased as time prolonged. The corrosion rate is 0.43 mm/year in static conditions compared to the slightly higher value of 0.34 mm/year for samples exposed to the flow at 188 rpm. After 48 hours of exposure, the corrosion rates in both static and dynamic conditions remain at approximately the same value of 0.15 mm/year. The results suggest that the small flow rate of 188 rpm at 200°C increased the general corrosion of super 13Cr SS in the first 5 hours; However, the recorded averaged corrosion rates in both static and dynamic conditions show no significant difference after 20 hours of exposure.

The decline in the averaged corrosion rate with time was measured for samples exposed to high p_{CO_2} of 28.5 bar in both static conditions and at a rotation speed of 188 rpm. The highest corrosion rate of 2.75 mm/year was recorded after 5 hours of exposure under static conditions. The corrosion rates under static conditions are higher compared to the 188 rpm conditions in the first 20 hours; However, the averaged corrosion rate under static conditions is approximately 1.3 times smaller than under the 188 rpm conditions after 48 hours of exposure. The paper presents the surface analysis results and the hypothesis that their differences are due to the nature of the corrosion scales that develop on the surface under the different conditions.

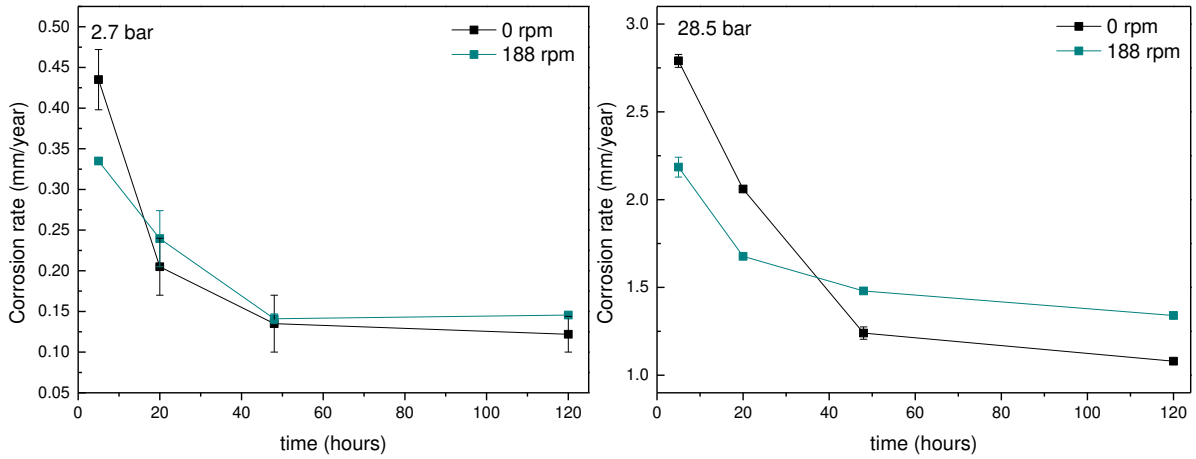

(a) (b)

Figure 2. Averaged corrosion rates of super 13Cr SS at various immersion times at 200°C and (a) 2.7 bar and (b) 28.5 bar CO_2.

Film formation and morphology observation at low p_{CO_2} of 2.7 bar

Figure 3 illustrates the top-view SEM images of the corrosion product evolution for super 13Cr SS exposed to CO_2-saturated solutions during various immersion times in static and under a rotation speed of 188 rpm. For the static conditions at 200°C, the steel surface was observed no sign of corrosion after 5 hours (Figure 3a), then was covered by randomly scattered crystals after 20 hours (Figure 3c). After 48 hours of exposure, the steel surface was covered by more crystalline grains (Figure 3e). It is interesting to note that larger crystals are randomly scattered on the entire surface after 120 hours (Figure 3g). Compared to static conditions, there is no obvious difference on the surface under a small flow rate of 188 rpm at various immersion times. No crystalline grains and the polishing marks were apparent on the steel surface after 120 hours as shown in Figures 3b, 3d, 3f, and 3h.

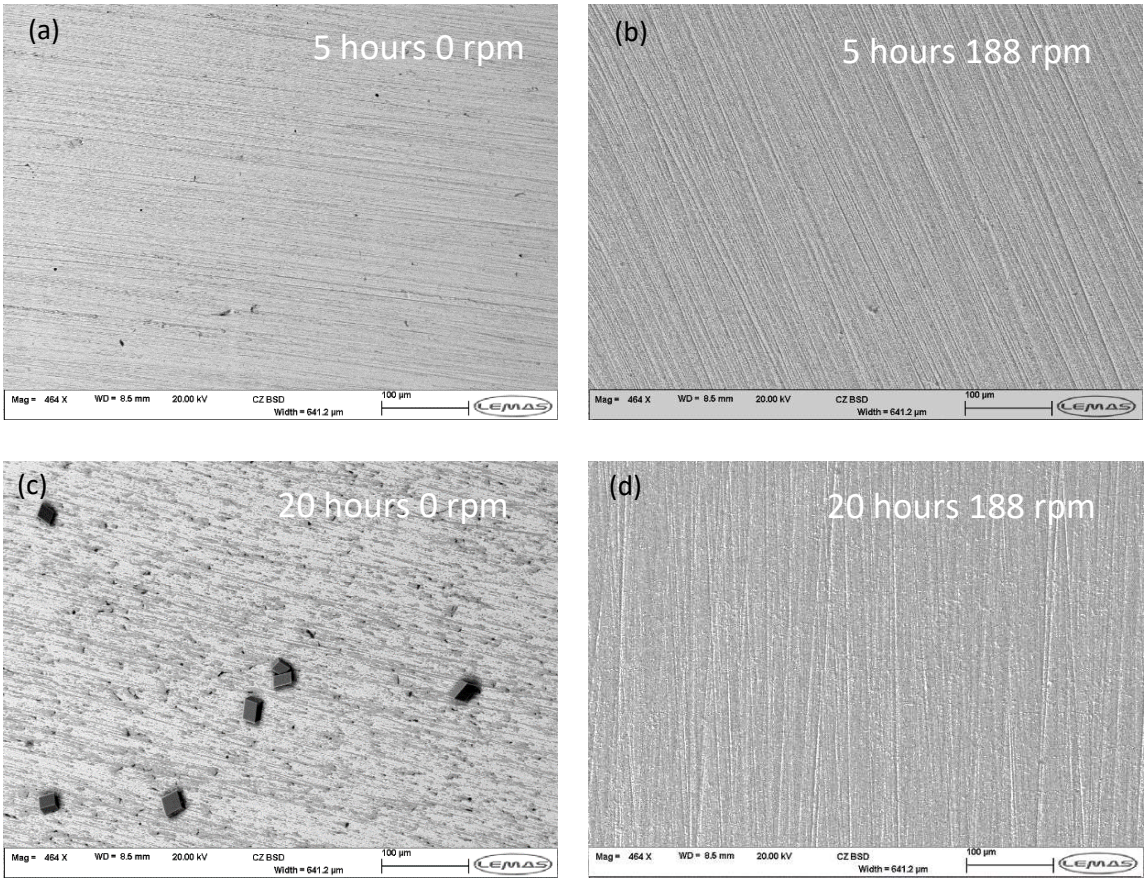

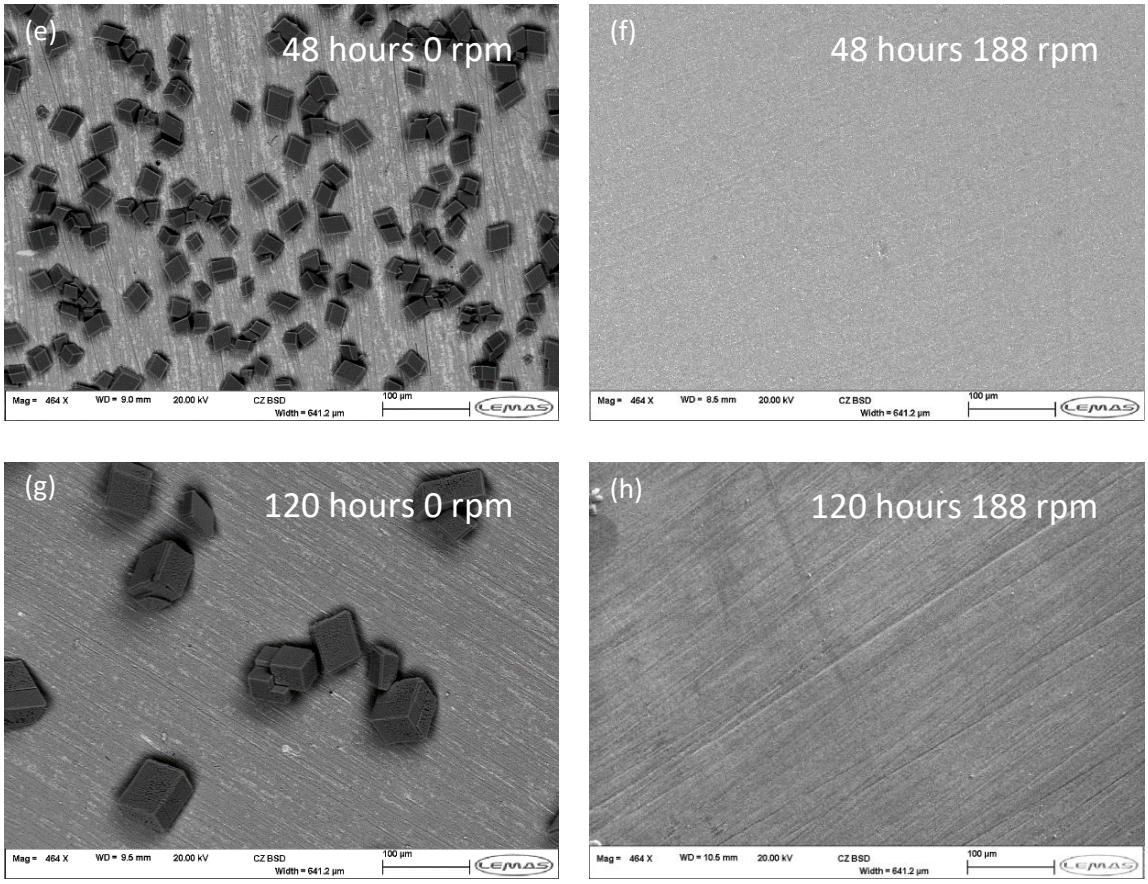

Figure 3. SEM images of the corrosion products at various immersion times at 200°C and 2.7 bar CO_2, (a)(c)(e)(g) – 0 rpm and (b)(d)(f)(h) – 188 rpm.

XRD measurement was performed to identify the development of crystalline corrosion scales at various immersion times with/without introducing a small flow rate of 188 rpm. As shown in Figure 4a, the corrosion products mainly comprise $FeCO_3$ and $FeCr_2O_4$ when the samples were exposed to static conditions. The results show that the crystalline $FeCO_3$ was detected in the early stages (5 hours) and the intensity of crystalline $FeCO_3$ increased with immersion times; However, no crystalline $FeCO_3$ was detected when the samples were exposed at the rotation speed of 188 rpm after 120 hours as shown in Figure 4b.

Raman measurement was used to identify the nature of the potential thin corrosion scales which the XRD was not able to detect. Figure 5 indicates the precipitate on the inner layer is mainly $FeCr_2O_4$ and the formation of $FeCr_2O_4$ was detected in both static conditions and under the rotation speed of 188 rpm conditions.

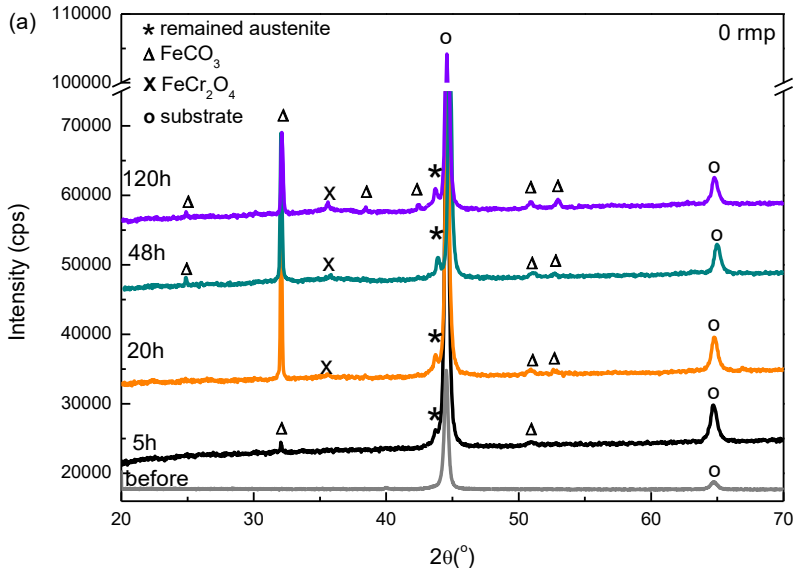

203

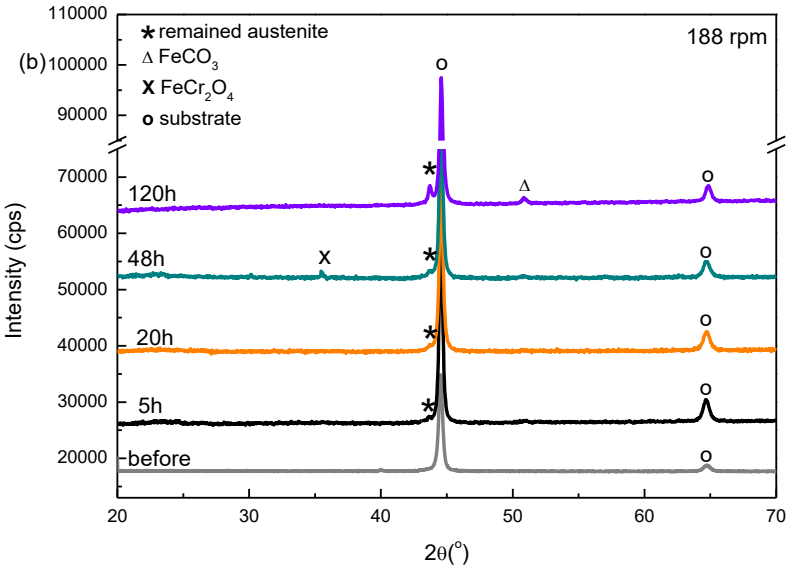

204

205 Figure 4. XRD patterns of super 13Cr SS specimens immersed in the solution (a) under static
206 conditions and (b) under rotation at 200°C and 2.7 bar CO_2 for 5, 20, 48, and 120 hours.

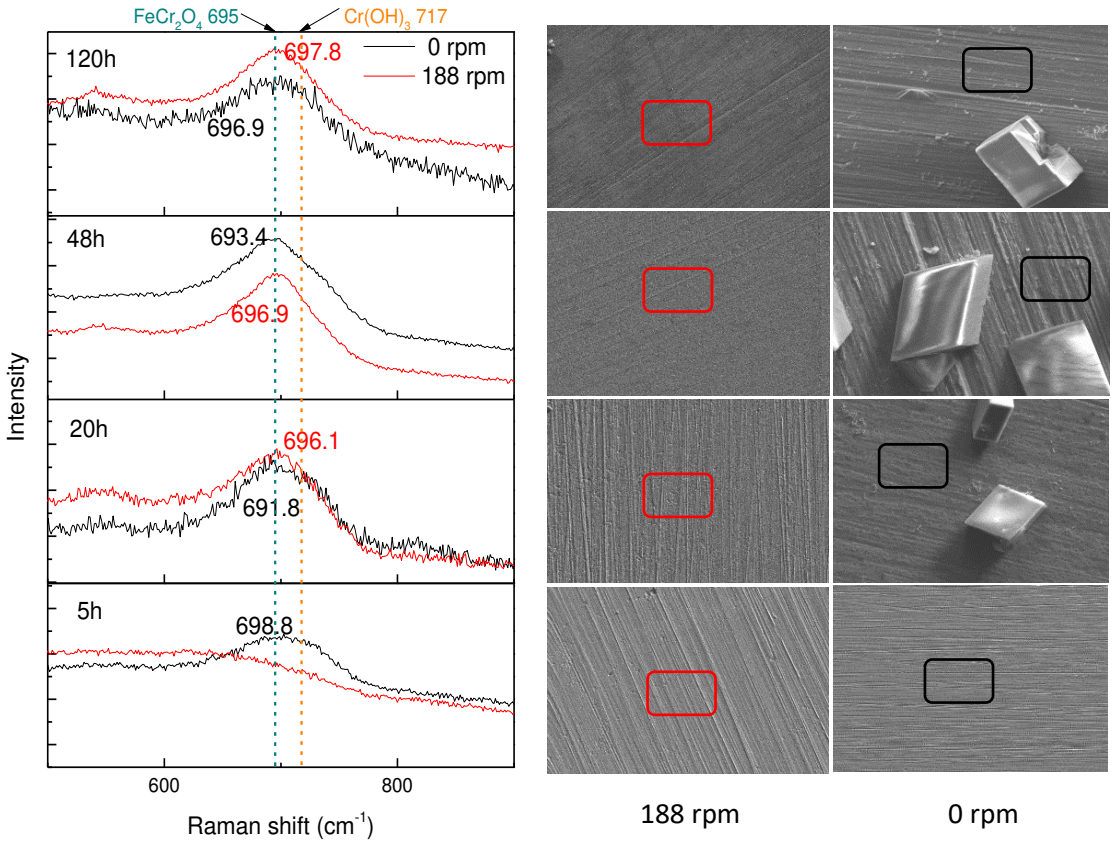

Figure 5. The detected Raman spectra for the development of the corrosion product scales at various immersion times at 200°C and 2.7 bar CO_2 under static and rotation speed of 188 rpm.

The cross-sectional SEM images of the corrosion product films formed on super 13Cr SS immersed in CO_2-saturated solution after 120 hours in both static conditions and under a rotation speed of 188 rpm are shown in Figure 6. The image in Figure 6a indicates that the corrosion products under static conditions have two layers: an inner non-uniform layer and an outer layer. Combined with XRD and Raman measurements, the corrosion products can be identified as an outer layer of crystalline $FeCO_3$ and an inner layer of mainly $FeCr_2O_4$. The inner $FeCr_2O_4$ layer is between 1.5 μm and 50 nm in thickness and this suggests that there is preferential dissolution occurred for the samples immersed in the solution under static conditions as the development of the corrosion products are not uniformly distributed.

The formation of the corrosion product layers on super 13Cr SS at a rotation speed of 188 rpm was relatively uniform compared to that of samples exposed to static conditions. The inner layer is uniformly covered on the surface and is about 300 nm in thickness. The EDS line

scans in both static and rotating conditions indicate that the inner layer comprises Fe, Cr, and O which is in agreement with the Raman results shown in Figure 5.

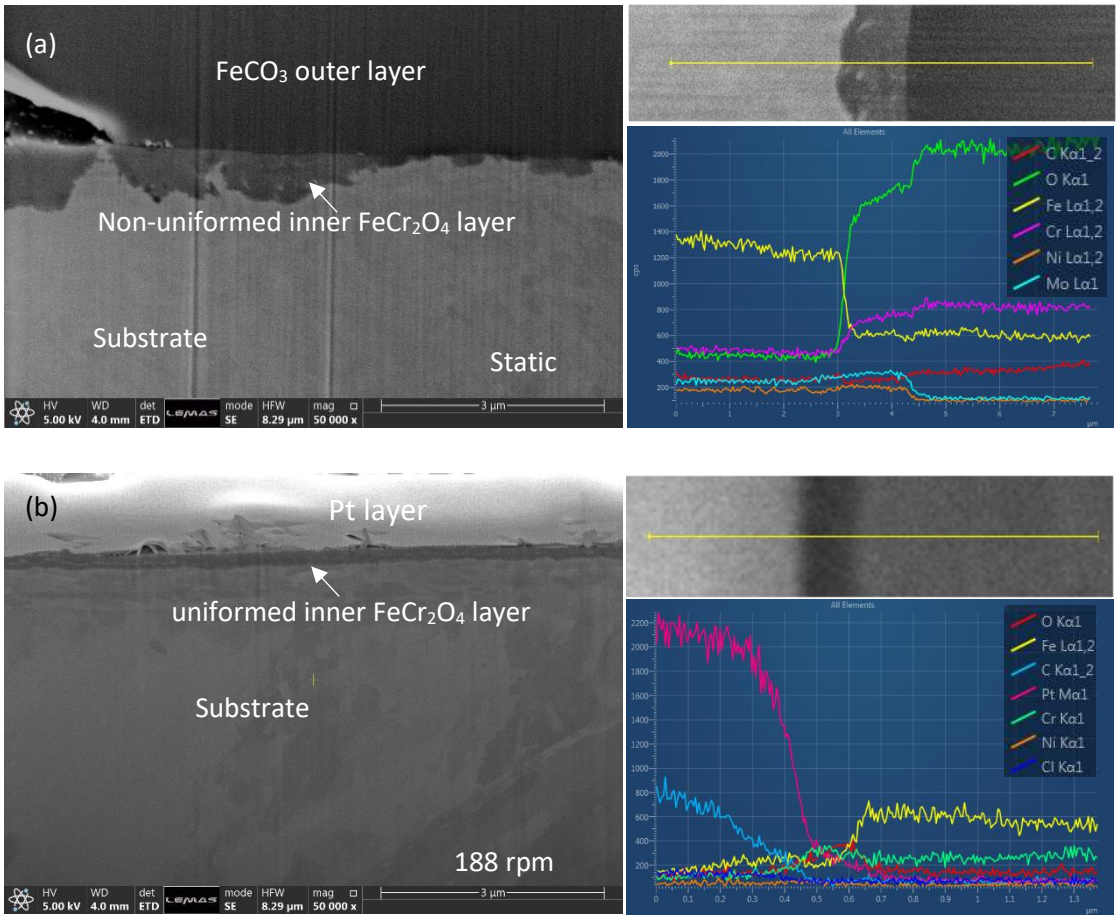

Figure 6. Chemical composition and structure of the corrosion product films formed on the 13Cr SS surface after 120 hours in static (a) and rotation speed of 188 rpm (b) at 200°C and 2.7 bar CO_2.

Film formation and morphology observation at high p_{CO2} of 28.5 bar

The morphology of the growth of the corrosion scales on the super 13Cr SS surface at various immersion times in both static and rotating conditions at high p_{CO2} of 28.5 bar is examined by SEM. In the case of the static conditions, the polishing marks were observed after 5 hours of exposure as shown in Figure 7a. Small numbers of cubic crystals are randomly distributed on the surface, which are identified as $FeCO_3$ by both Raman and XRD analysis as shown in Figure 8 and Figure 9 after 20 hours. Increasing the immersion time to 48 hours (Figure 7e) resulted in the formation of more quantities of crystalline $FeCO_3$; However, it is interesting to note that the gaps are still visible between the crystalline $FeCO_3$ after 120 hours of exposure.

Under the rotating speed of 188 rpm, the SEM images indicate that the increase in flow speed delayed the development of crystalline $FeCO_3$ on the surface compared to static conditions. The polishing marks are still visible after 20 hours. Traces of crystalline $FeCO_3$, confirmed by Raman and XRD measurements are shown in Figure 8 and Figure 9 after 48 hours of exposure time. The results suggest that the small flow rate suppressed the crystalline $FeCO_3$ precipitation on the super 13Cr SS steel.

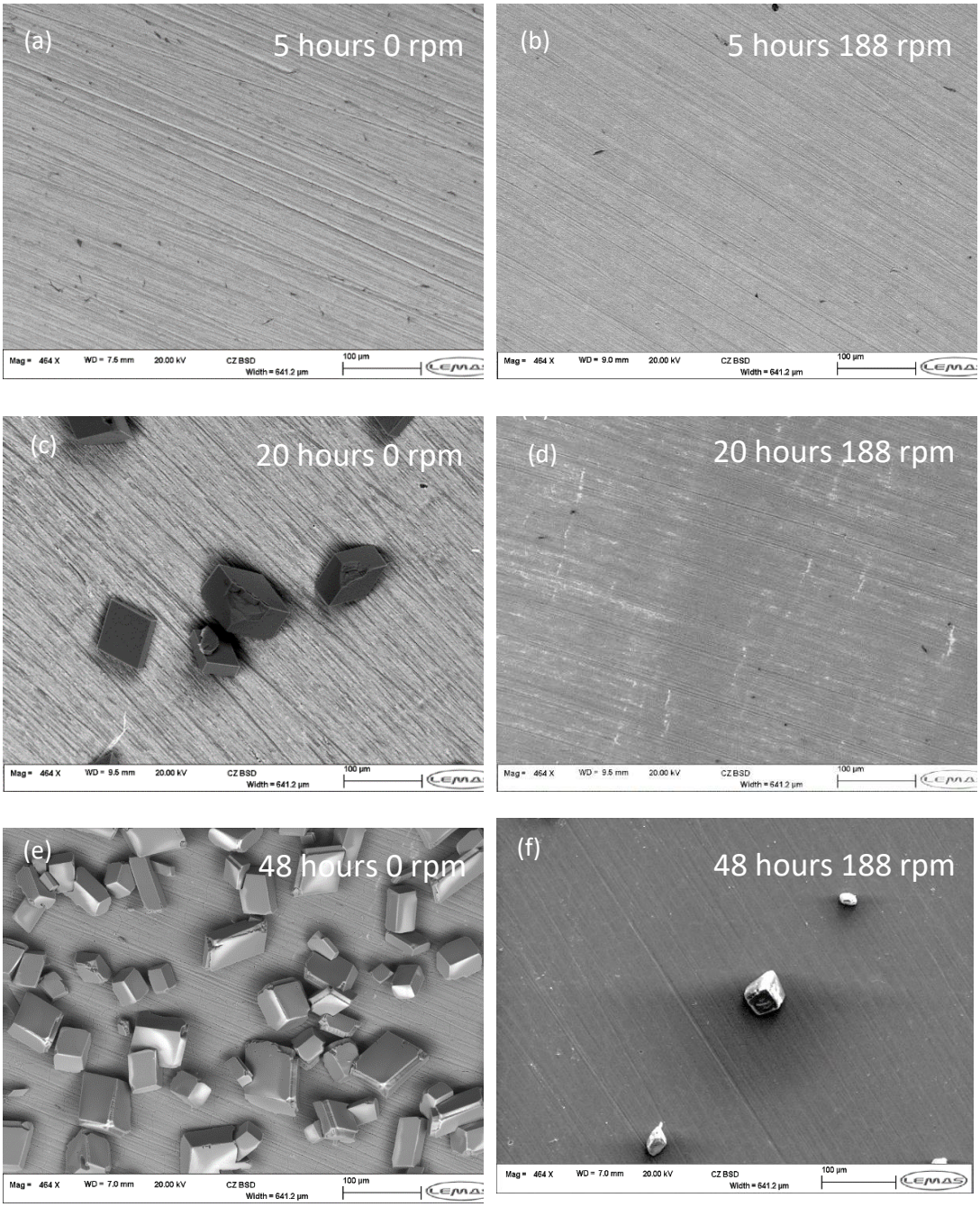

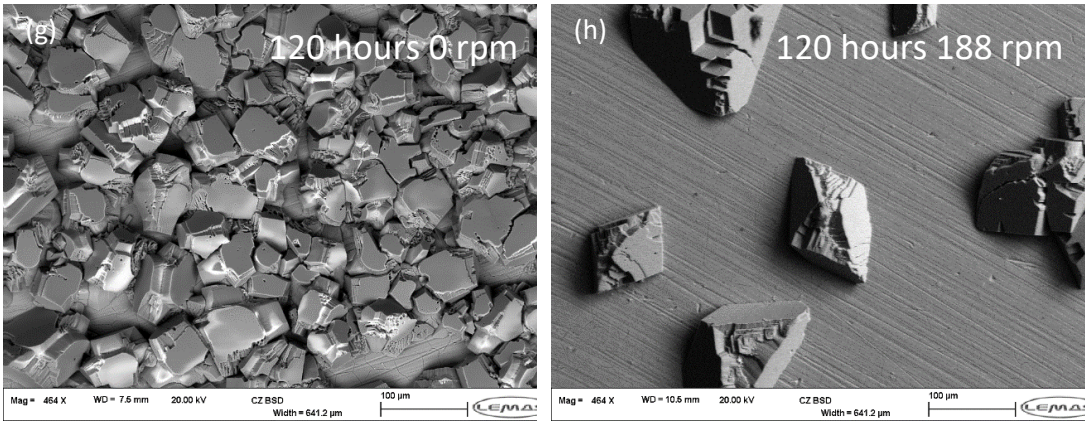

Figure 7. SEM images of the development of corrosion products at various immersion times at 200°C and 28.5bar CO_2.

Figure 8 presents the XRD pattern of the corrosion products formed on the surface at various immersion times in both static conditions and under rotation. The presence of crystalline $FeCO_3$ is confirmed in Figure 8. The iron peak (45°) in both static conditions and under rotation disappeared after 120 hours, suggesting that the development of corrosion scales is sufficiently thick and X-rays cannot detect to the steel substrate.

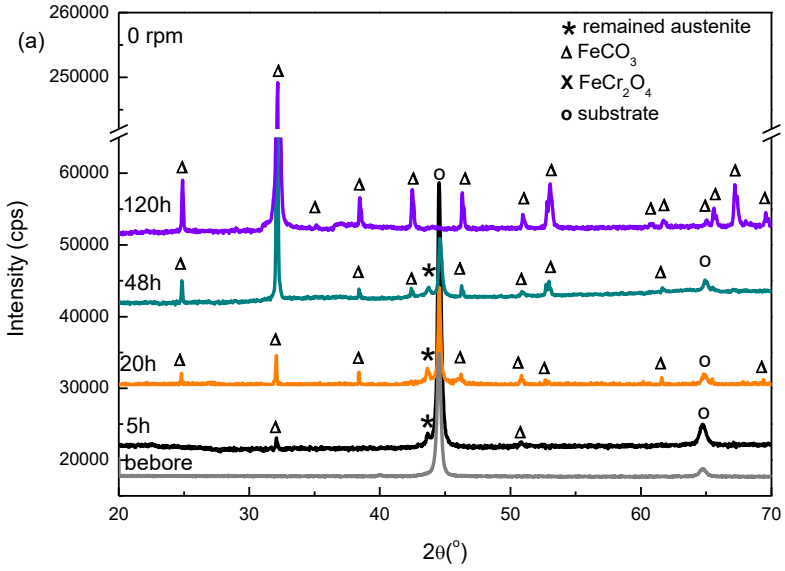

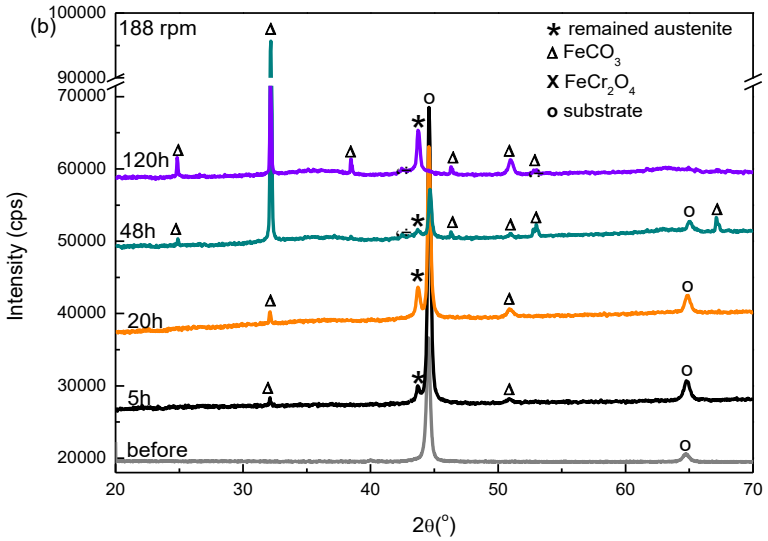

Figure 8. XRD patterns of the super 13Cr SS specimens immersed in the solution (a) under static conditions and (b) under rotation at 200 °C for 5, 20, 48, and 120 hours.

The presence of the inner layer was confirmed by analysis of the Raman spectra as shown in Figure 9. The Raman spectra of the inner layer indicate that the corrosion products are mainly $Cr(OH)_3$ at various immersion times in static conditions. With a small flow rate, an inner layer of $FeCr_2O_4$ was detected after the first 5 hours. The Raman results indicate a shift in the peak positions with increased immersion time, gradually shifted the peak from 707 cm^{-1} to 717 cm^{-1} between 5 hours and 120 hours. This suggests that the corrosion products change from $FeCr_2O_4$ to $Cr(OH)_3$ on the surface after a longer immersion time.

For the static conditions, it becomes apparent that the development of corrosion products on the surface consists of crystalline $FeCO_3$ as an outer layer and an inner layer of $Cr(OH)_3$. Under rotation, the situation is different and the corrosion products consist of $FeCO_3$, $Cr(OH)_3$, and $FeCr_2O_4$.

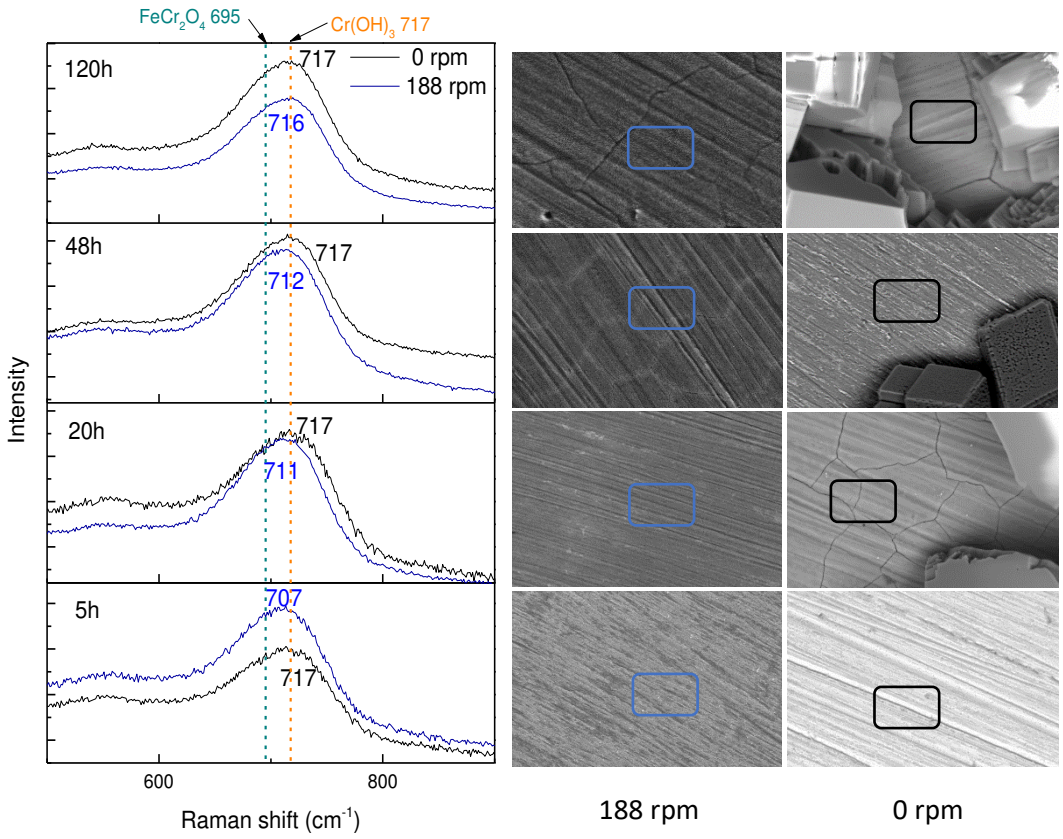

Figure 9. The detected Raman spectra for the development of the corrosion product scales at 200°C and 28.5 bar CO_2 under static and rotation speed of 188 rpm.

The cross-sectional SEM images of the corrosion product films on super 13Cr SS exposed after 120 hours in the static and rotating conditions are shown in Figure 10. The thickness of the inner layer formed under static conditions (Figure 10a) is less consistent than in dynamic conditions (Figure 10b). The inner layer ranges from 5 to 20 µm in thickness for the static conditions. The inner layer underneath the crystalline $FeCO_3$ is slightly thinner than the uncovered regions for the rotation speed of 188 rpm.

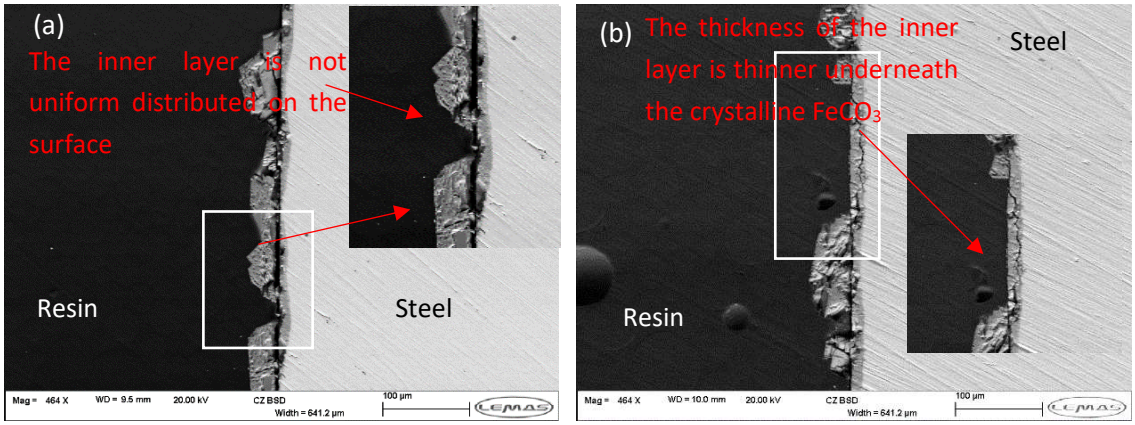

Figure 10. Cross-sectional images of the corrosion products formed on super 13Cr SS surface in static (a) and rotation speed of 188 rpm (b) at 200°C and 28.5 bar CO_2.

The chemical composition of the growth of the corrosion product layers on super 13Cr SS surface exposed to CO_2-saturated solution after 120 hours in both static and rotating conditions are further examined by FIBs/EDS. The inner layer contains two phases in both static conditions and rotating conditions, presenting as the gray and the scattered light gray spots. According to the EDX elemental analyses, the chemical composition of the gray region (spectrum 2) detects Cr and O confirmed as $Cr(OH)_3$ by the Raman spectra shown in Figure 9. The light gray spots within the corrosion products have similar elements compared to the steel substrate which is identified as austenite based on XRD measurements as shown in Figure 8. The line scan results further confirmed that the elemental composition of the inner corrosion product layer mainly contains iron, chromium, nickel, and oxygen, whereas the scattered light gray spots indicate less oxygen but rich in nickel and iron.

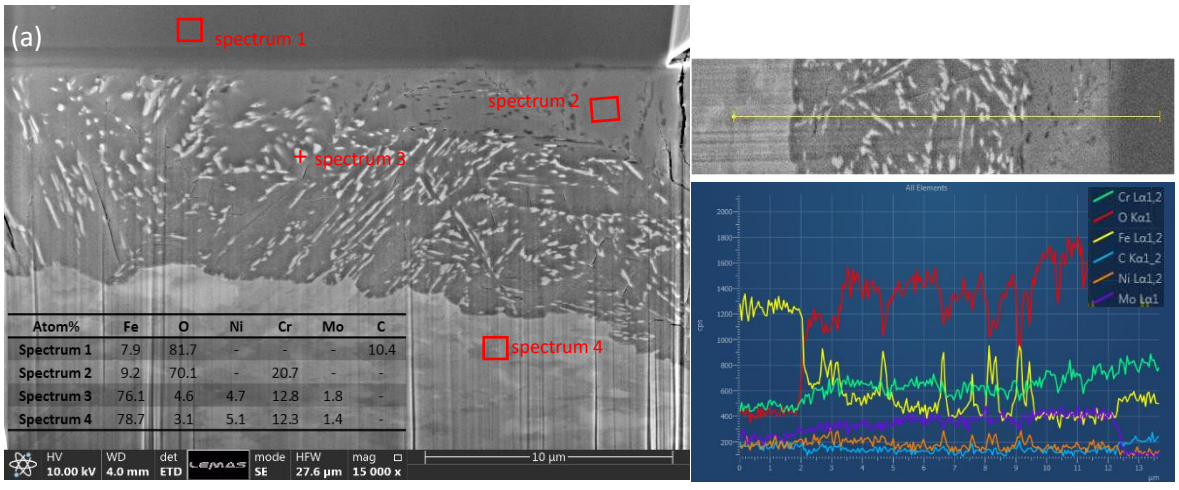

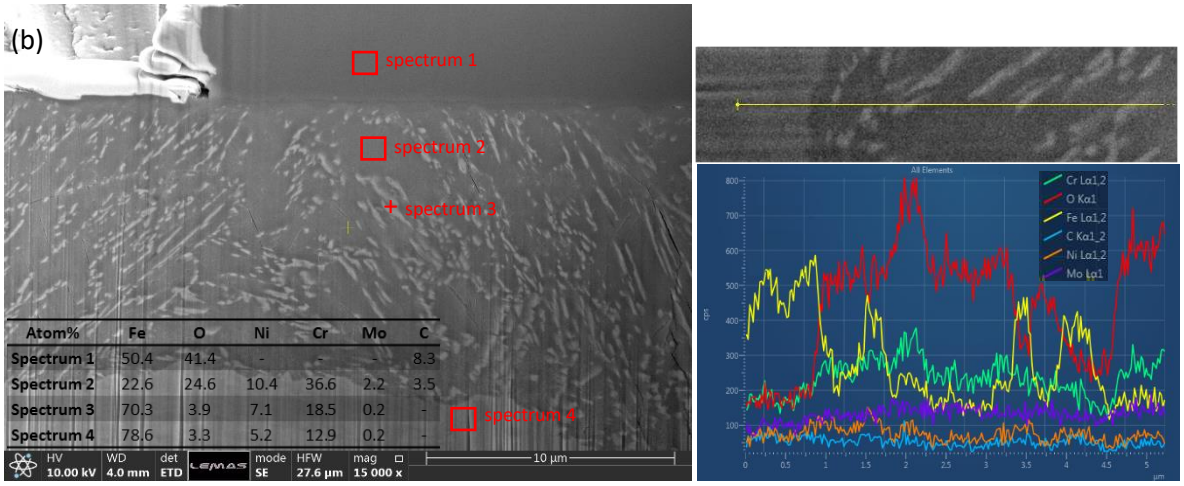

291

292 Figure 11. Elemental composition of the corrosion product films formed on super 13Cr SS in
293 static (a) and rotation speed of 188 rpm (b) at 200°C and 28.5 bar CO_2.
294

295 ***Localised corrosion behaviours in static and 188 rpm conditions***

296 The corrosion scales were removed according to ASTM G 01-03, profilometry was performed
297 on the surface. The averaged localised/pitting depths in Figure 12 are calculated considering
298 the top 10 deepest pits. In the static and low p_{CO_2} of 2.7 bar conditions, the localised/pitting
299 depth increased from 2.43 to 11.64 µm between 5 hours and 120 hours, and suggests that
300 the localised pits were continuously growth on the super 13Cr surface. Conversely, the
301 averaged localised pitting depths maintained relatively stable, the localised pit depth of 5µm
302 was measured after 120 hours at the rotation speed of 188rpm. The results indicate that the
303 calculated localised corrosion rates under the static condition were higher than those at 188
304 rpm. The addition of the flow rate reduced the localised pitting corrosion under the test
305 condition here.

306 There is a notable increase in the average pit depth with time for samples exposed to the high
307 p_{CO_2} of 28.5 bar in both static and rotating conditions compared to that of low p_{CO_2} of 2.7 bar.
308 The highest localised corrosion rate was 5.35 mm/year after 5 hours and reduced to 2.1
309 mm/year after 120 hours for static conditions. The dynamic condition exhibited a lower
310 localised corrosion rate of 4.5 mm/year for the first 5 hours and reduced to 0.5 mm/year after
311 120 hours. The results suggest that the localised corrosion rates under static conditions were
312 higher than in dynamic conditions.

According to Figure 12, the results indicate that the localised corrosion rates are approximately 10 times higher than the averaged corrosion rates, suggesting that localised corrosion represents a real threat to pipeline integrity under the test conditions here.

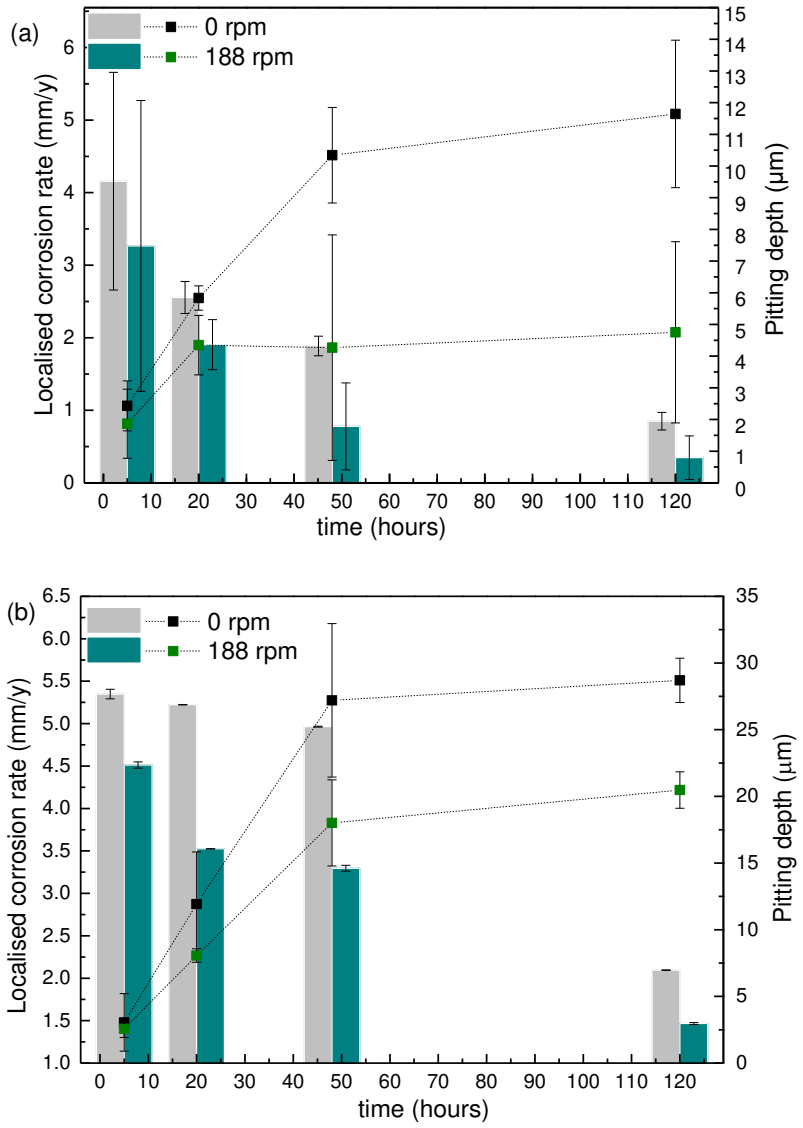

Figure 12. Pit depths of super 13Cr SS at various immersion times at 200°C and (a) 2.7 bar and (b) 28.5 bar CO_2.

Figure 13 provides the examples of 2D profilometry images of 3 mm x 3 mm scanned area and the SEM images from the super 13Cr SS sample surface after removing the corrosion products. The results shown in Figure 13a exhibit that super 13Cr SS suffered localised corrosion attack at 200°C and p_{CO_2} of 2.7 bar under static conditions after 120 hours of exposure. A number of small localised/pits were detected on the surface as shown in Figure 13c. There is no deep

localised corrosion attack for samples exposed to the rotation speed of 188rpm as shown in Figure 13b. These results are in good agreement with the measurement of the pit depth as shown in Figure 12a, the pit depth in static conditions are two or three times higher than that of the dynamic conditions at the same temperature of 200°C and p_{CO_2} of 2.7 bar after 120 hours of exposure.

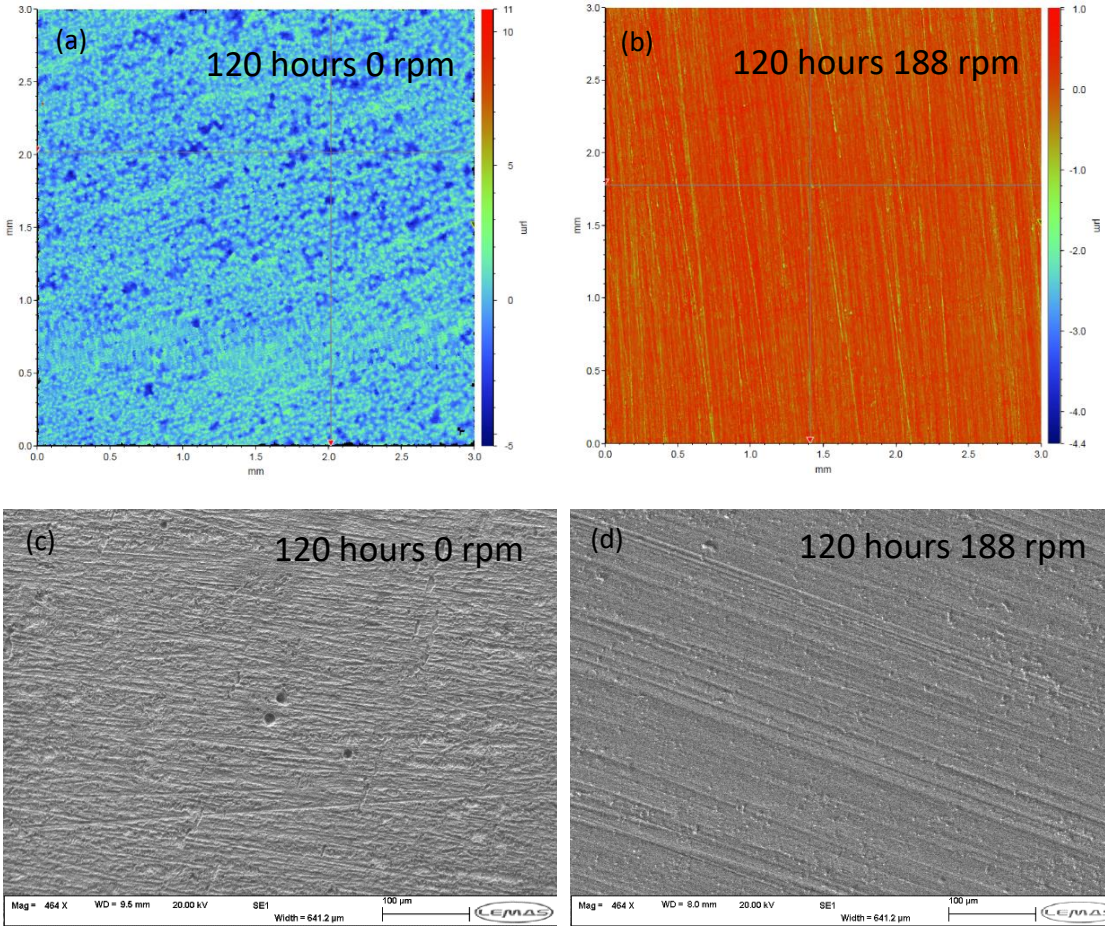

Figure 13. 2D Profilometry and SEM images of corroded super 13Cr SS samples at 200°C and 2.7 bar of CO_2 after removing the corrosion products (a – 120 hours in static, b – 120 hours in 188 rpm, c – the pits morphology after 120 hours in static and d - the pits morphology after 120 hours in 188 rpm.

Compared to the low p_{CO_2} of 2.7 bar, samples suffered more severe localised corrosion attack as p_{CO_2} was increased to 28.5 bar as expected. The results agreed with the observation of deeper and more pitting attack from the profilometry images as shown in Figure 14. Deeper localised/pits of 10µm were measured on the surface after 20 hours exposed to the static condition. From the surface profiles between 48 and 120 hours as shown in Figure 14, the

morphology of localised/pitting corrosion was small and deep (Figure 14 e and g), compared to the wider and open localised attack observed when the test condition changed from static to the rotation speed of 188 rpm conditions (Figure 14 f and h).

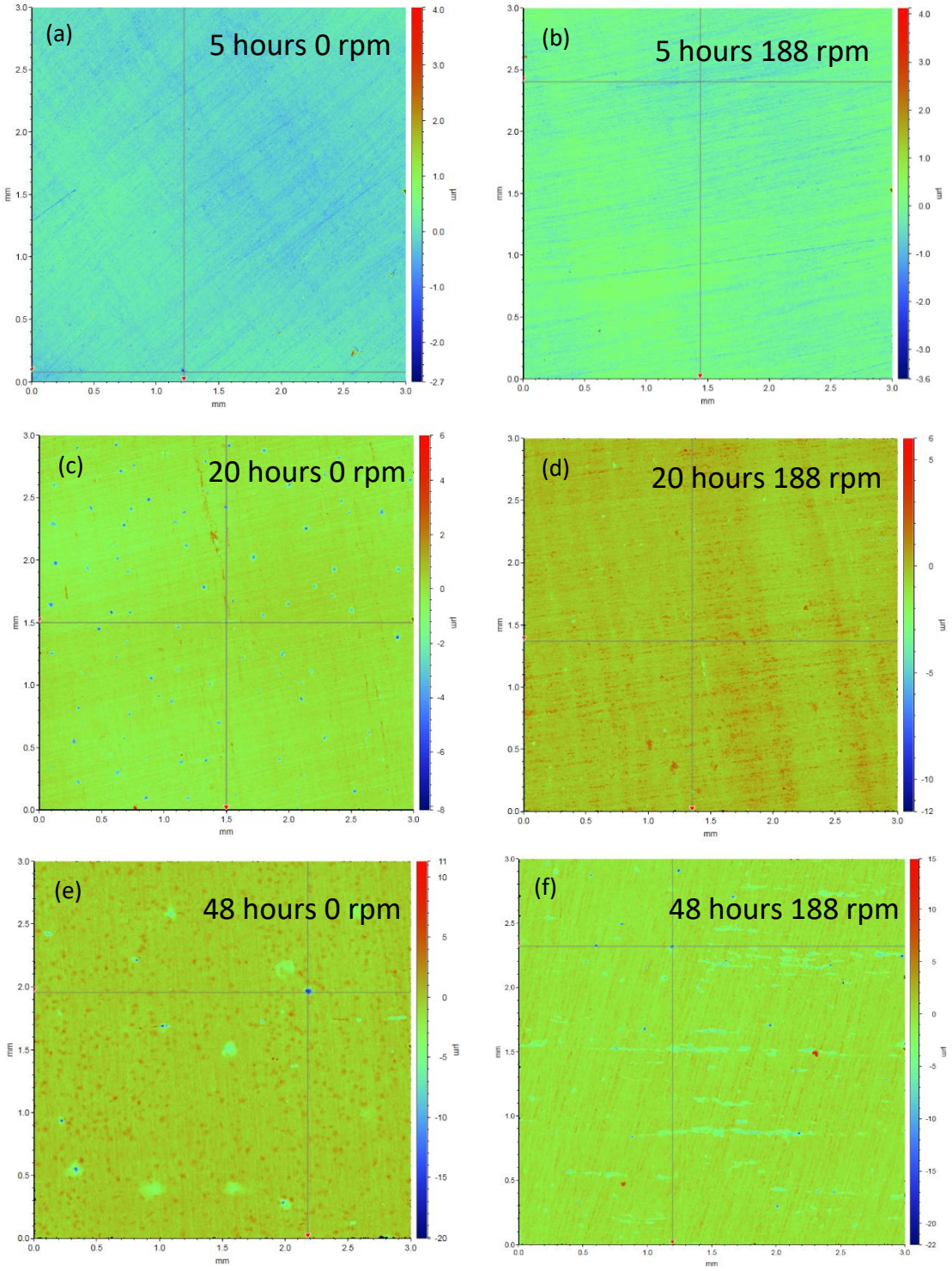

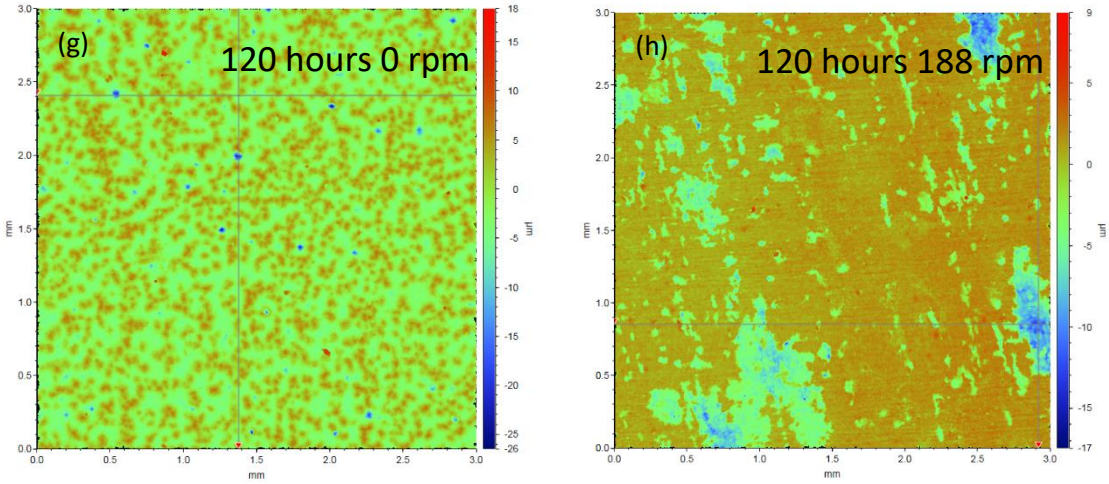

342 Figure 14. 2D Profilometry images of corroded super 13Cr SS samples exposed at various
343 immersion times at 200°C and 28.5 bar of CO_2. (after removing the corrosion products).

344 Figure 15 exhibits the SEM images of the corroded sample surface (after removing the
345 corrosion products) at 200°C and 28.5 bar CO_2. The results indicate that the pitting became
346 deeper with the increase in the immersion time for the static conditions, whereas the
347 observed pitting corrosion elongated along the flow direction under the rotation speed of 188
348 rpm condition. After 120 hours of exposure, the observed pitting on the surface under static
349 conditions was markedly deeper (Figure 15c), while the observed pitting attack on the surface
350 under flow conditions was wider and shallow as shown in Figure 15d.

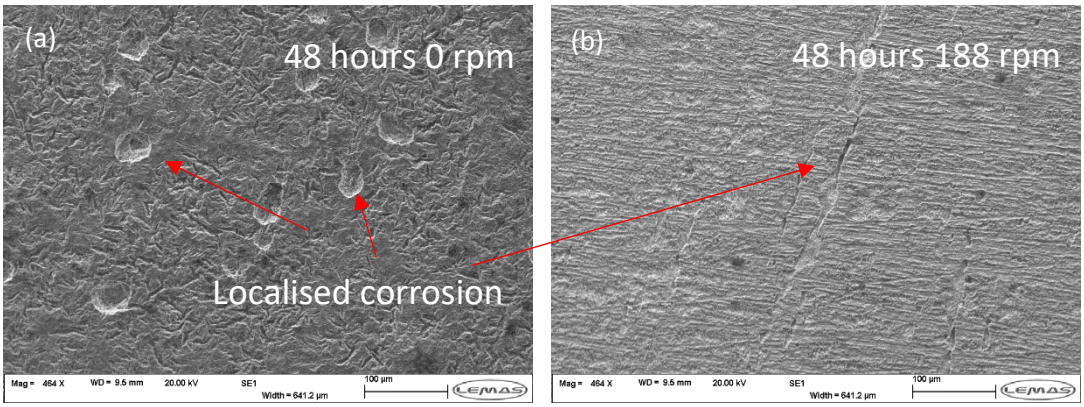

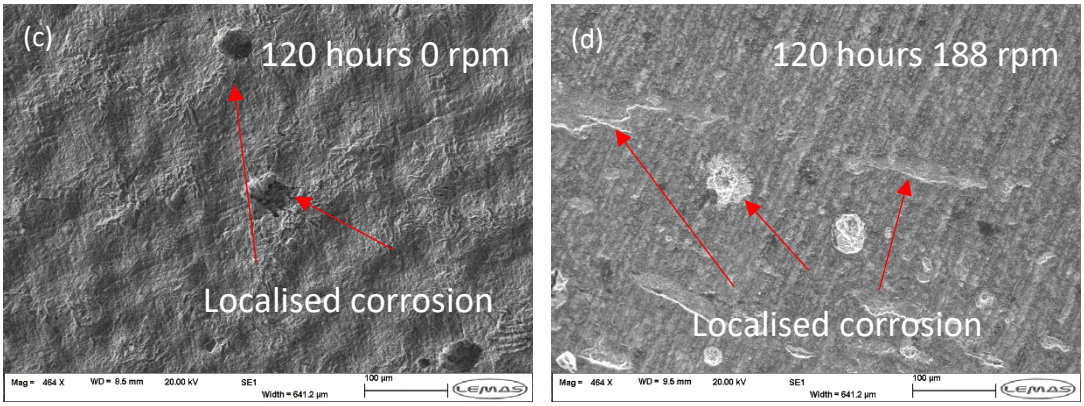

Figure 15. SEM images of corroded super 13Cr SS samples exposed for (a) (b) 48 hours and (c) (d) 120 hours at 200°C and 28.5 bar of CO_2. (after removing the corrosion products).

Discussion

Effect of small flow velocity on the growth of multilayer corrosion products at p_{CO_2} of 2.7 bar

At 200°C and p_{CO_2} of 2.7 bar, the development of the $FeCr_2O_4$ layer significantly decreased the averaged corrosion rates of super 13Cr SS (Figure 2a) in both static and dynamic conditions. The multilayered corrosion scales have been discussed in previous sections. The high corrosion rates in the first 5 hours indicated that super 13Cr SS does not achieve passivity at p_{CO_2} of 2.7 bar and 200°C. The passive film on the surface was partially dissolved because of the high temperature and pressure conditions which accelerated the transport of metal ions outward [14]. The dissolved sites acted as an anode and the diffused Fe^{2+} partially replaced the octahedral sites of Cr^{3+} within Cr_2O_3 on the surface, forming the $FeCr_2O_4$ layer by reactions (4)-(6) [14,43]. The generated hydrogen ions during the corrosion processes are consumed via corresponding cathodic reactions as follows [23,37]:

$$2e^- + 2H^+ \rightarrow H_2 \quad (10)$$

$$2H_2CO_3 + 2e^- \rightarrow H_2 + 2HCO_3^- \quad (11)$$

$$2HCO_3^- + 2e^- \rightarrow H_2 + 2CO_3^{2-} \quad (12)$$

Reactions (11) plays an important role due to the relatively large amount of H_2CO_3 in the aqueous phase. The generation of hydrogen ions via reactions (4)-(6) at the metal/inner layer interface is responsible for the decrease in pH value, while the cathode releases an equivalent amount of alkalinity and increases the pH via reactions (10)-(12).

The formation of the crystalline $FeCO_3$ outer layer is affected by the corrosion kinetics via the $FeCO_3$ supersaturation. The crystalline $FeCO_3$ precipitated on the outer layer was driven by the level of supersaturation (*SR*):

$$SR = \frac{[Fe^{2+}][CO_3^{2-}]}{K_{SP}} \quad (13)$$

where K_{sp} represents the solubility product for $FeCO_3$ (mol^2/L^2), $[Fe^{2+}]$ and $[CO_3^{2-}]$ are the concentration of Fe^{2+} and CO_3^{2-}, respectively [44]. It has been stated that the $FeCO_3$ formation rate is greatly promoted only when a critical supersaturation ratio (SR_c) is being exceeded [45]. The crystalline $FeCO_3$ increased in number in the period of 48 hours of exposure and then grew in size from 48 to 120 hours. Previous research reported that the nucleation rate increases exponentially with *SR*, and particle growth rate increases linearly with relative *SR* [15], suggesting the nucleation is dominant only when *SR* reaches a high level. The development of scattered, big $FeCO_3$ crystals over 120 hours in 2.7 bar CO_2 condition indicates the inner $FeCr_2O_4$ layer is relatively compact with few defects for ions transfer and increased the crystal growth.

Additionally, it is worth noting that the growth of the corrosion product multilayers at p_{CO_2} of 2.7 bar was affected by the rotation speed of 188 rpm. The small velocity appears to take away the metal ions at the material interface, which minimised the preferential development of the inner $FeCr_2O_4$ layer compared with the formation of the non-uniform $FeCr_2O_4$ layer for the static conditions. Secondly, the effect of flow delayed the Fe^{2+} and CO_3^{2-} to reach the SR_c, resulting in the delayed precipitation of the crystalline $FeCO_3$ on the surface.

The corrosion product film-induced the localised corrosion at p_{CO_2} of 2.7 bar

Figure 16a exhibits that the corroded super 13Cr SS surface was rugged and attacked by the localised/pitting corrosion in the static conditions at p_{CO_2} of 2.7 bar, compared to the relatively flat corroded surface under the rotation speed of 188 rpm (Figure 16b).

Based on the discussion above, the inner layer which is primarily composed of $FeCr_2O_4$ has been identified as the key component against the general corrosion. It has been widely accepted that the occurrence of pitting under the passivation state was caused by large cathode coupled with a small anode [46]. During the corrosion processes at the substrate

400 interface, the hydrogen ions generate and accumulate, which leads to a drop of the corrosion
401 potential and keep the dissolution sites as an anode. The preferential growth of the inner
402 $FeCr_2O_4$ layer on the surface indicated that the regions covered by the $FeCr_2O_4$ layer became
403 the cathode, and the growth rate of $FeCr_2O_4$ was suppressed because of the alkalinity
404 released by the cathode. Moreover, after reaching the SR_c, the crystalline $FeCO_3$ precipitated
405 and presented as a barrier, turning the covered surface to the cathode, which elevated the
406 risk of the localised corrosion by the crystalline $FeCO_3$ covered sites with lower corrosion rate
407 than uncovered regions, as shown in Figure 16c.
408 However, the small velocity promoted to the removal of the hydrogen ions at the interface
409 during the formation of $FeCr_2O_4$, which accelerated the diffusion of hydrogen ions and
410 elevated the corrosion potential at the scale/substrate interface, avoiding the propagation of
411 localised corrosion, as shown in Figure 16d. Besides, the delayed precipitation of crystalline
412 $FeCO_3$ under the dynamic conditions prevented the increase in cathode areas on the surface
413 as well as the development of the localised corrosion.

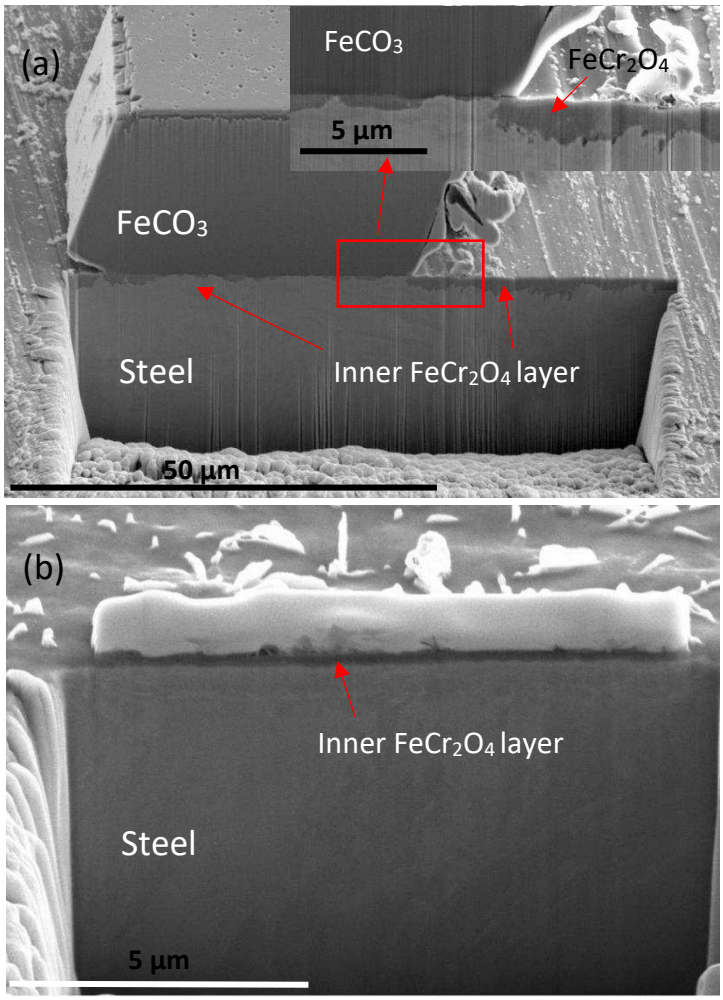

Figure 16. Schematic diagram of the inner corrosion product film-induced the localised corrosion at 200°C and 2.7 bar of CO_2 conditions: (a)(c) static, (b)(d) rotation speed of 188 rpm.

Effect of small flow velocity on the growth of porous corrosion product layers at p_{CO_2} of 28.5 bar

At 200°C and p_{CO_2} of 28.5 bar, the corrosion rate reached 2.8 mm/year in the first 5 hours, compared to the measured corrosion rate of 0.43 mm/year at 2.7 bar p_{CO_2}. $FeCr_2O_4$ and

$Cr(OH)_3$ were thermodynamically stable corrosion products as the p_{CO_2} increased to 28.5 bar [43]. The inner corrosion layer was mainly $Cr(OH)_3$ (confirmed by Raman as shown in Figure 8), which was proved to form via the precipitation reactions [47]:

$$Cr^{3+} + 3H_2O \rightarrow Cr(OH)_3 + 3H^+ \quad (14)$$

As shown in Figure 11, the inner layer coexisted with small quantities of the undissolved metal substrate, which suggests that the corrosion products grew inward the substrate. The undissolved metals within the inner corrosion product layer confirmed as the retained austenite by XRD (Figure 8), presenting a better corrosion resistance than the martensite phase [48]. During the corrosion processes, the martensite phase with poor corrosion resistance preferentially dissolved; the amorphous $Cr(OH)_3$ filled the dissolved martensite substrate and covered the undissolved austenite, forming the inner layer. The complicated structure of the inner layer resulted in a relatively loose barrier with more defects for ions transfer than that of the $FeCr_2O_4$ layer formed on the surface at lower p_{CO_2}.

The precipitation of the outer crystalline $FeCO_3$ occurred once the Fe^{2+} and CO_3^{2-} reaching the supersaturation, and it influenced the cations transfer to the steel substrate. The super 13Cr SS surface was not fully covered by the crystalline $FeCO_3$, suggesting that the covered regions were corroded slower than the uncovered regions, which in agreement with the observation of the cross-sectional SEM images as shown in Figure 9a, the localised corrosion was observed at uncovered regions.

Based on the previous reports, the propagation of the localised/pitting corrosion was caused by acidification in a small anode. Two reactions mainly influence the pH value under the condition of high p_{CO_2}, one is the corrosion reaction which released an equivalent amount of alkalinity and increases the pH [23]:

$$2M + nH_2CO_3 \rightarrow 2M^{n+} + nH_2 + 2nHCO_3^- \quad (15)$$

The other is the precipitation reactions of $FeCO_3$ and $Cr(OH)_3$ via reaction (7) – (8), and (14), which consume CO_3^{2-} and OH^- and decrease pH [8,49]. Therefore, acidification occurred where the precipitation rate was higher than the corrosion rate.

Under the rotation speed of 188 rpm conditions, the previous discussion suggests that the small flow speed contributed to the development of the uniform inner layer, indicating an

equilibrium between anodic dissolution and precipitation of the inner layer. The SEM image (Figure 7h) also proved the small velocity has an effect to delay the precipitation of the outer crystalline $FeCO_3$ occurring on the surface with p_{CO_2} of 28.5 bar and suppress the growth of scattered outer corrosion product layer.

Porous corrosion product film-induced the localised corrosion at p_{CO_2} of 28.5 bar

As shown in Figure 13, the effect of the small flow speed affected the localised/pitting morphology which transformed from the deep-hole shape to the shallow-disk shape during the 120 hours of exposure, suggesting the propagation of the localised corrosion was affected by the small velocity at 200°C and 28.5 bar of p_{CO_2}.

The precipitation of the defective inner $Cr(OH)_3$ layer acted as a barrier and reduced the corrosion rates for the static conditions. At a longer time, the inner layer was gradually covered with $FeCO_3$ crystals, and the uncovered regions have low corrosion protection with preferentially corrosive species penetration sites, resulting in the localised corrosion occurring as shown in Figure 17 a and c.

On the contrary, the effect of the flow is to delay the precipitation of the crystalline $FeCO_3$ onto the inner $Cr(OH)_3$ layer, as shown in Figure 17 b. The flow velocity promoted the metal ion transfer and the elevated cation ions penetrated through the $Cr(OH)_3$ layer caused by the high corrosion rates. The porous and defective inner $Cr(OH)_3$ layer grows inward and constantly transports Fe^{2+} ions outwards. Ultimately, the accumulated Fe^{2+} concentration reaches supersaturation and form scattered $FeCO_3$ crystals (Figure 17d). Mobbassar et al. [50] reported the crucial of local microenvironments and local fluctuations in the mass-transport rate. According to the previous research done by Zhao et al. [51], a concave semicircle of 5 μm can generate vortex with low flow rates in a dynamic condition. For this study, after 120 hours of immersion at 200°C and 28.5 bar of p_{CO_2}, the precipitation of $FeCO_3$ crystals turned the uncovered region as a concave with about 10 μm in depth, resulting in a relatively asymmetric distribution of H^+ ions as shown in Figure 17d. The localised corrosion occurs at the precipitated regions of porous $Cr(OH)_3$ due to the acidification, and the level of H^+ ions accumulates at upstream which widen the pits along the flow direction, forming pits with disk-like shape as shown in Figure 14h and Figure 15d.

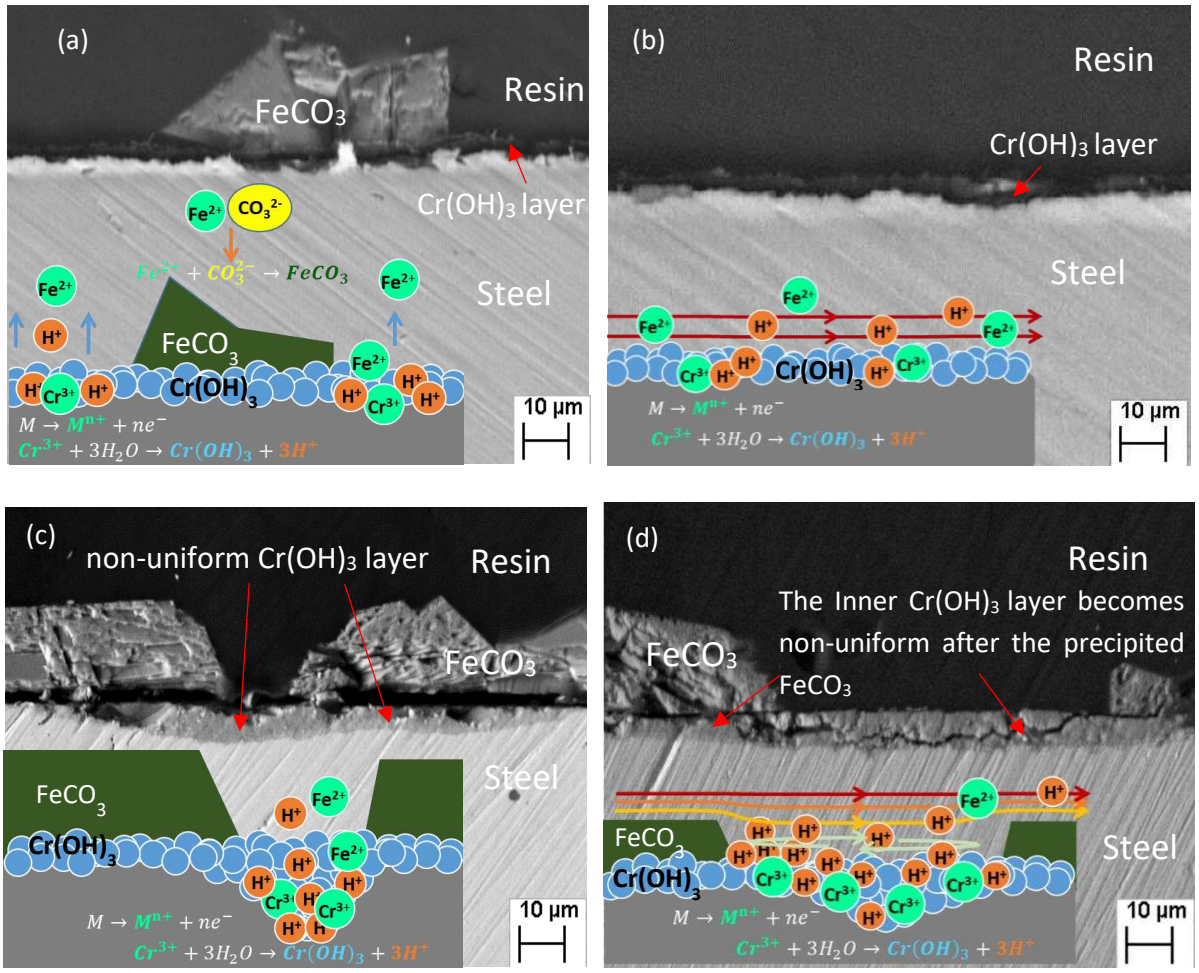

Figure 17. Schematic diagram of the porous corrosion product film-induced localised corrosion at 200°C and 28.5 bar CO_2 conditions (a) 5 hours in static (b) 5 hours in rotation speed of 188 rpm, (c) 120 hours in static (d) 120 hours in rotation speed of 188 rpm.

Conclusions

The growth mechanism of corrosion scales and localised corrosion behaviour of super 13Cr SS immersed in a CO_2-saturated 4.86 wt. % NaCl brine at 200°C has been investigated at various p_{CO2} in static conditions and a rotation speed of 188rpm respectively. The following main conclusions can be made:

1. The development of the inner corrosion product layer on super 13Cr SS at 200°C and p_{CO2} of 2.7 bar mainly contained $FeCr_2O_4$, which presents as a rugged tomography in static conditions and became uniform at the rotation speed of 188 rpm respectively.
2. The formation of the crystalline outer $FeCO_3$ layer was randomly distributed in static

conditions over 120 hours of immersion time compared with no observed crystalline $FeCO_3$ at the rotation speed of 188 rpm after 120 hours at 200°C and p_{CO_2} of 2.7 bar.

3. For the condition of p_{CO_2} of 28.5 bar, the inner corrosion product layer displayed the composite structure comprising amorphous $Cr(OH)_3$ coexisting with undissolved austenite in both static and dynamic conditions.
4. The small flow rate reduced the localised corrosion measurements at both p_{CO_2} of 2.7 bar and 28.5 bar. In the case of low p_{CO_2} of 2.7 bar, the reduction in the localised corrosion was attributed to the formation of a uniform and dense $FeCr_2O_4$ inner layer. As the p_{CO_2} increased to 28.5 bar, the geometry of the pitting transformed from the deep-hole shape to the shallow-disk shape after 120 hours of exposure.

Reference

[1] E. Sikora, D.D. Macdonald, Defining the passive state, Solid State Ion. 94 (1997) 141–150.

[2] T. Moffat, R. Latanision, An electrochemical and X-Ray photoelectron spectroscopy study of the passive state of chromium, J. Electrochem. Soc. 139 (1992) 1869–1879.

[3] B. Lovreček, J. Sefaja, Semiconducting aspects of the passive layer on chromium, Electrochimica Acta. 17 (1972) 1151–1155.

[4] K. Asami, K. Hashimoto, S. Shimodaira, An XPS study of the passivity of a series of iron—chromium alloys in sulphuric acid, Corros. Sci. 18 (1978) 151–160.

[5] I. Olefjord, B.-O. Elfstrom, The composition of the surface during passivation of stainless steels, Corrosion. 38 (1982) 46–52.

[6] Y. Hua, S. Mohammed, R. Barker, A. Neville, Comparisons of corrosion behaviour for X65 and low Cr steels in high pressure CO2-saturated brine, J. Mater. Sci. Technol. 41 (2020) 21–32.

[7] H. Amaya, T. Mori, K. Kondo, H. Hirata, M. Ueda, others, Effect of chromium and molybedenum on corrosion resistance of super 13Cr martenistic stainless steel in CO2 environment, in: Corros. 98, NACE International, Paper No. 98113, 1998.

[8] Y. Hua, R. Jonnalagadda, L. Zhang, A. Neville, R. Barker, Assessment of general and localized corrosion behavior of X65 and 13Cr steels in water-saturated supercritical CO2 environments with SO2/O2, Int. J. Greenh. Gas Control. 64 (2017) 126–136.

[9] K. Kondo, M. Ueda, K. Ogawa, H. Amaya, H. Hirata, H. Takabe, Y. Miyazaki, Alloy design of super 13 Cr martensitic stainless steel(development of super 13 Cr martensitic stainless steel for line pipe-1), Supermartensitic Stainl. Steels99. (1999) 11–18.

[10] L.T. Popoola, A.S. Grema, G.K. Latinwo, B. Gutti, A.S. Balogun, Corrosion problems during oil and gas production and its mitigation, Int. J. Ind. Chem. 4 (2013) 35.

[11] X. Yue, M. Zhao, L. Zhang, H. Zhang, D. Li, M. Lu, Correlation between electrochemical properties and stress corrosion cracking of super 13Cr under an HTHP CO 2 environment, RSC Adv. 8 (2018) 24679–24689.
[12] A. Turnbull, A. Griffiths, Corrosion and cracking of weldable 13 wt-% Cr martensitic stainless steels for application in the oil and gas industry, Corros. Eng. Sci. Technol. 38 (2003) 21–50.
[13] S. Jin, A. Atrens, ESCA-Studies of the structure and composition of the passive film formed on stainless steels by various immersion temperatures in 0.1 M NaCl solution, Appl. Phys. A. 45 (1988) 83–91.
[14] X. Yue, L. Zhang, Y. Wang, S. Xu, C. Wang, M. Lu, A. Neville, Y. Hua, Evolution and characterization of the film formed on super 13Cr stainless steel in CO2-saturated formation water at high temperature, Corros. Sci. 163 (2020) 108277. https://doi.org/10.1016/j.corsci.2019.108277.
[15] M. Gao, X. Pang, K. Gao, The growth mechanism of CO2 corrosion product films, Corros. Sci. 53 (2011) 557–568.
[16] Y. Zhao, X. Li, C. Zhang, T. Zhang, J. Xie, G. Zeng, D. Xu, F. Wang, Investigation of the rotation speed on corrosion behavior of HP-13Cr stainless steel in the extremely aggressive oilfield environment by using the rotating cage test, Corros. Sci. 145 (2018) 307–319.
[17] J. Robertson, The mechanism of high temperature aqueous corrosion of stainless steels, Corros. Sci. 32 (1991) 443–465.
[18] R. Moreira, C. Franco, C. Joia, S. Giordana, O. Mattos, The effects of temperature and hydrodynamics on the CO2 corrosion of 13Cr and 13Cr5Ni2Mo stainless steels in the presence of free acetic acid, Corros. Sci. 46 (2004) 2987–3003.
[19] Y. Zhao, J. Xie, G. Zeng, T. Zhang, D. Xu, F. Wang, Pourbaix diagram for HP-13Cr stainless steel in the aggressive oilfield environment characterized by high temperature, high CO2 partial pressure and high salinity, Electrochimica Acta. 293 (2019) 116–127.
[20] L. Mu, W. Zhao, Investigation on carbon dioxide corrosion behaviour of HP13Cr110 stainless steel in simulated stratum water, Corros. Sci. 52 (2010) 82–89.
[21] A. Tyurin, The Diagram of Electrochemical Equilibrium of 12X18H10T Steel, Prot. Met. 40 (2004) 240–248. https://doi.org/10.1023/B:PROM.0000028916.29742.89.
[22] S. Guo, D. Xu, N. Wei, Y. Wang, G. Chen, S. Wang, Oxidation Processes and Involved Chemical Reactions of Corrosion-Resistant Alloys in Supercritical Water, Ind. Eng. Chem. Res. XXXX (2020). https://doi.org/10.1021/acs.iecr.0c01394.
[23] A. Dugstad, others, Fundamental aspects of CO2 metal loss corrosion-part 1: mechanism, in: Corros. 2006, Nace International, San Diego, CA, 2006.
[24] D. D. H., B. G. T., The Effects of Bicarbonate on the Corrosion and Passivation of Iron, CORROSION. 36 (1980) 416–422.
[25] Y. Hua, R. Barker, A. Neville, Effect of temperature on the critical water content for general and localised corrosion of X65 carbon steel in the transport of supercritical CO2, Int. J. Greenh. Gas Control. 31 (2014) 48–60.
[26] S. Zhang, L. Hou, H. Du, H. Wei, B. Liu, Y. Wei, A study on the interaction between chloride ions and CO2 towards carbon steel corrosion, Corros. Sci. 167 (2020) 108531. https://doi.org/10.1016/j.corsci.2020.108531.

[27] S. Zhang, L. Hou, H. Du, H. Wei, B. Liu, Y. Wei, Synergistic Contribution of Chloride and Bicarbonate Ions to Pitting Corrosion Behavior of Carbon Steel, CORROSION. 75 (2019) 1034–1043. https://doi.org/10.5006/3195.
[28] S. Zhang, L. Hou, H. Du, H. Wei, B. Liu, Y. Wei, An electrochemical study on the effect of bicarbonate ion on the corrosion behaviour of carbon steel in CO2 saturated NaCl solutions, Vacuum. 167 (2019) 389–392. https://doi.org/10.1016/j.vacuum.2019.06.038.
[29] D.D. Macdonald, The history of the point defect model for the passive state: a brief review of film growth aspects, Electrochimica Acta. 56 (2011) 1761–1772.
[30] J. Töpfer, S. Aggarwal, R. Dieckmann, Point defects and cation tracer diffusion in (CrxFe1- x) 3-δO4 spinels, Solid State Ion. 81 (1995) 251–266.
[31] H. Zhang, Y. Zhao, Z. Jiang, Effects of temperature on the corrosion behavior of 13Cr martensitic stainless steel during exposure to CO2 and Cl- environment, Mater. Lett. 59 (2005) 3370–3374.
[32] P. Wang, N. Xiao, S. Lu, D. Li, Y. Li, Investigation of the mechanical stability of reversed austenite in 13% Cr–4% Ni martensitic stainless steel during the uniaxial tensile test, Mater. Sci. Eng. A. 586 (2013) 292–300.
[33] Xiaowei Lei, Yaorong Feng, Jianxun Zhang, Anqing Fu, Chengxian Yin, Digby D Macdonald, Impact of Reversed Austenite on the Pitting Corrosion Behavior of Super 13Cr Martensitic Stainless Steel, Electrochimica Acta. 191 (2016) 640–650.
[34] X. Li, Y. Zhao, W. Qi, J. Xie, J. Wang, B. Liu, G. Zeng, T. Zhang, F. Wang, Effect of extremely aggressive environment on the nature of corrosion scales of HP-13Cr stainless steel, Appl. Surf. Sci. 469 (2019) 146–161.
[35] J. Heuer, J.F. Stubbins, Microstructure analysis of coupons exposed to carbon dioxide corrosion in multiphase flow, Corrosion. 54 (1998) 566–575.
[36] Y. Hua, R. Barker, T. Charpentier, M. Ward, A. Neville, Relating iron carbonate morphology to corrosion characteristics for water-saturated supercritical CO2 systems, J. Supercrit. Fluids. 98 (2015) 183–193.
[37] S. Nesic, J. Postlethwaite, S. Olsen, An electrochemical model for prediction of corrosion of mild steel in aqueous carbon dioxide solutions, Corrosion. 52 (1996) 280–294.
[38] J. Han, S. Nešić, Y. Yang, B.N. Brown, Spontaneous passivation observations during scale formation on mild steel in CO2 brines, Electrochimica Acta. 56 (2011) 5396–5404.
[39] Y. Hua, S. Xu, Y. Wang, W. Taleb, J. Sun, L. Zhang, R. Barker, A. Neville, The formation of FeCO3 and Fe3O4 on carbon steel and their protective capabilities against CO2 corrosion at elevated temperature and pressure, Corros. Sci. 157 (2019) 392–405.
[40] TM 0177 N S. Standard Test Method, Laboratory Testing of Metals for Resistance to Sulfide Stress Cracking and Stress Corrosion Cracking in H2S Environments., ASTM international, 2016.
[41] Mutiscale 7.1 is a commercial software package from Expro Group Internatioal Ltd, for more information see: http://mutiscale.no/., n.d.
[42] A.C.G.-1 on C. of Metals, Standard practice for preparing, cleaning, and evaluating corrosion test specimens, ASTM international, 2011.
[43] X. Yue, L. Zhang, C. Sun, S. Xu, C. Wang, M. Lu, A. Neville, Y. Hua, A thermodynamic and kinetic study of the formation and evolution of corrosion product scales on 13Cr stainless steel in a geothermal environment, Corros. Sci. (2020) 108640.

[44] E. Van Hunnik, B.F. Pots, E. Hendriksen, The formation of protective FeCO3 corrosion product layers in CO2 corrosion, NACE International, Houston, TX (United States), Paper No. 6, 1996.
[45] S. Guo, L. Xu, L. Zhang, W. Chang, M. Lu, Corrosion of alloy steels containing 2% chromium in CO2 environments, Corros. Sci. 63 (2012) 246–258.
[46] Y. Tsutsumi, A. Nishikata, T. Tsuru, Pitting corrosion mechanism of Type 304 stainless steel under a droplet of chloride solutions, Corros. Sci. 49 (2007) 1394–1407.
[47] S. Guo, L. Xu, L. Zhang, W. Chang, M. Lu, Characterization of corrosion scale formed on 3Cr steel in CO2-saturated formation water, Corros. Sci. 110 (2016) 123–133.
[48] S. Zhang, P. Wang, D. Li, Y. Li, Investigation of the evolution of retained austenite in Fe–13% Cr–4% Ni martensitic stainless steel during intercritical tempering, Mater. Des. 84 (2015) 385–394.
[49] Y. Hua, R. Barker, G. Bermperidis, H. Zhao, L. Zhang, A. Neville, Comparison of corrosion behavior of X65, 1Cr, 5Cr and 13Cr steels in water-containing supercritical CO2 environments with SO2/O2, in: Proc. Corros. 2016, Leeds, 2016.
[50] M.H. Sk, A.M. Abdullah, M. Ko, B. Ingham, N. Laycock, R. Arul, David.E. Williams, Local supersaturation and the growth of protective scales during CO2 corrosion of steel: Effect of pH and solution flow, Corros. Sci. 126 (2017) 26–36. https://doi.org/10.1016/j.corsci.2017.05.026.
[51] Y. Zhao, L. Chang, T. Zhang, J. Xie, Y. Chen, D. Xu, F. Wang, Effect of the Flow Velocity on the Corrosion Behavior of UNS S41426 Stainless Steel in the Extremely Aggressive Oilfield Environment for the Tarim Area, CORROSION. 76 (2020) 654–665. https://doi.org/10.5006/2813.